Druitt, T.H., Kutterolf, S., Ronge, T.A., and the Expedition 398 Scientists
Proceedings of the International Ocean Discovery Program Volume 398
publications.iodp.org

Site U1598[1]

Keywords
International Ocean Discovery Program, IODP, R/V *JOIDES Resolution*, Expedition 398, Hellenic Arc Volcanic Field, Earth Connections, Earth in Motion, Biosphere Frontiers, Site U1598, Santorini caldera, Aegean Sea, Christiana-Santorini-Kolumbo volcanic field, subduction zone, shallow-marine volcanism

Core descriptions

Supplementary material

References (RIS)

MS 398-112
Published 30 July 2024

Funded by NSF OCE1326927, ECORD, and JAMSTEC

S. Kutterolf, T.H. Druitt, T.A. Ronge, S. Beethe, A. Bernard, C. Berthod, H. Chen, S. Chiyonobu, A. Clark, S. DeBari, T.I. Fernandez Perez, R. Gertisser, C. Hübscher, R.M. Johnston, C. Jones, K.B. Joshi, G. Kletetschka, O. Koukousioura, X. Li, M. Manga, M. McCanta, I. McIntosh, A. Morris, P. Nomikou, K. Pank, A. Peccia, P.N. Polymenakou, J. Preine, M. Tominaga, A. Woodhouse, and Y. Yamamoto[2]

[1] Kutterolf, S., Druitt, T.H., Ronge, T.A., Beethe, S., Bernard, A., Berthod, C., Chen, H., Chiyonobu, S., Clark, A., DeBari, S., Fernandez Perez, T.I., Gertisser, R., Hübscher, C., Johnston, R.M., Jones, C., Joshi, K.B., Kletetschka, G., Koukousioura, O., Li, X., Manga, M., McCanta, M., McIntosh, I., Morris, A., Nomikou, P., Pank, K., Peccia, A., Polymenakou, P.N., Preine, J., Tominaga, M., Woodhouse, A., and Yamamoto, Y., 2024. Site U1598. In Druitt, T.H., Kutterolf, S., Ronge, T.A., and the Expedition 398 Scientists, Hellenic Arc Volcanic Field. Proceedings of the International Ocean Discovery Program, 398: College Station, TX (International Ocean Discovery Program). https://doi.org/10.14379/iodp.proc.398.112.2024
[2] **Expedition 398 Scientists' affiliations.**

1. Background and objectives

Site U1598 (proposed Site 14A) is located ~8 km northwest of Christiana Island and ~20 km southwest of Santorini (Figure **F1**) at 521.5 meters below sea level (mbsl). The drill site targeted the volcano-sedimentary fill of the Christiana Basin in two holes (U1598A and U1598B), with a maximum recovery depth of 95.7 meters below seafloor (mbsf) (all depths below seafloor are given using the core depth below seafloor, Method A [CSF-A], scale, except in **Operations** where the drilling depth below seafloor [DSF] scale is used) and core recoveries of 69% and 34%, respectively.

The drill site targeted the volcano-sedimentary fill of the Christiana Basin. This basin was believed to have formed by subsidence along an ENE–WSW fault system before the changing tectonic regime activated the current northeast–southwest rift system in which the Christiana-Santorini-Kolumbo (CSK) volcanic field lies (Tsampouraki-Kraounaki and Sakellariou, 2018; Preine et al.,

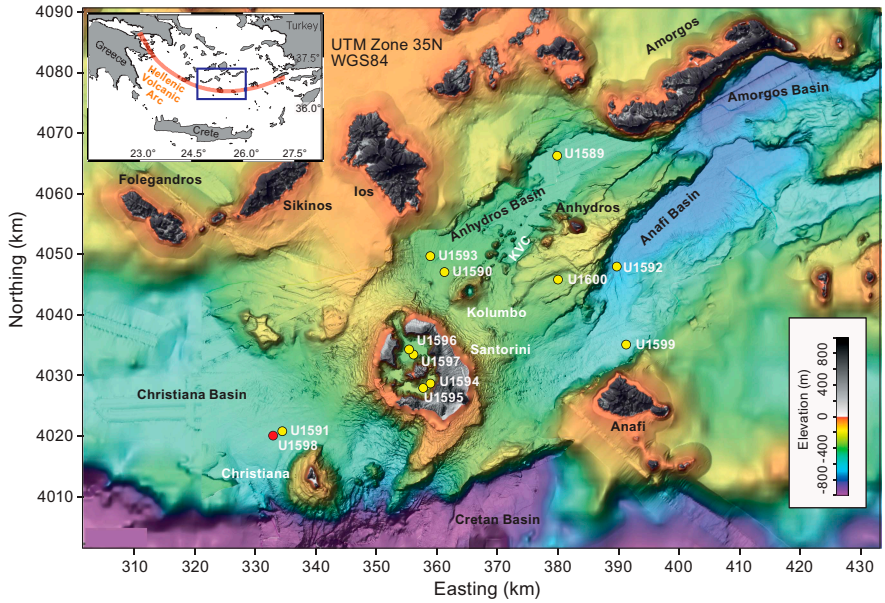

Figure F1. Site map. Red = Site U1598, yellow = other sites. Inset = location map. See Figure F1 in the Site U1589 chapter (Druitt et al., 2024a) for the swath data on which this map is based. KVC = Kolumbo volcanic chain.

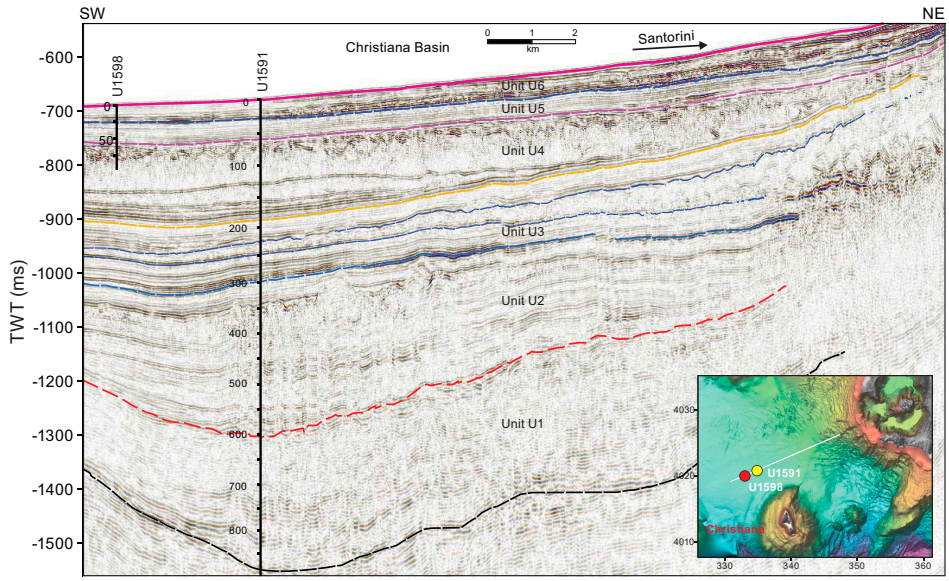

Figure F2. Seismic profile across the Christiana Basin along Seismic Line Geomar_P5009. The basin fill has six seismic stratigraphic units (U1–U6), following Preine et al. (2022b). Inset: location of Sites U1598 and U1591 in the same basin. Depths in meters. TWT = two-way traveltime.

2022a, 2022b). The Christiana Basin is deeper than the Anhydros and Anafi Basins; its volcanosedimentary fill potentially recorded the earlier volcanic history of the CSK volcanic field (including the products of Christiana and early Santorini), as well as the younger Santorini and possibly the Milos Volcano to the west along the Hellenic volcanic arc. The now-extinct Christiana Volcano produced lavas and tuffs of unknown ages (Aarburg and Frechen, 1999). An ignimbrite found on Christiani Island (one of the two small islands of the Christiana Volcano), Santorini, and the nonvolcanic island of Anaphi, called the Christiani Ignimbrite, was identified (Keller et al., 2010).

Site U1598 was chosen to complement the previously drilled Site U1591. The aim was to retarget a thick pumice layer found at Site U1591 (uppermost ~65 mbsf; Figure **F2**), for which we had insufficient samples for our scientific aims, to increase our recovery of the interval. The site addresses scientific Objectives 1–4 and 6 of the Expedition 398 Scientific Prospectus (Druitt et al., 2022).

2. Operations

The vessel arrived at Site U1598 on 24 January 2023 at 1945 h. The vessel was under full dynamic positioning (DP) control at 2015 h, ending the transit and marking the start of Site U1598.

2.1. Hole U1598A

The advanced piston corer/extended core barrel (APC/XCB) bottom hole assembly (BHA) with a bit was assembled. Hole U1598A (36°18.2937′N, 25°7.7155′E) was spudded at 2350 h on 24 January 2023 from 527.0 meters below rig floor (mbrf). Core 1H recovered 3.7 m, establishing the seafloor at 521.5 mbsl (Table **T1**). Coring continued on 25 January through Core 8H from 60.7 mbsf. The switch was made to the half-length APC (HLAPC) system with Cores 9F–10F at 70.2 mbsf. High torque was observed when drilling; the drill string was worked, but to be conservative the decision was made to pull out of the hole. The drill string was tripped up and out of the hole, and the bit cleared the seafloor at 0715 h, ending Hole U1598A.

2.2. Hole U1598B

The vessel was offset 50 m southwest from Hole U1598A. Hole U1598B (36°18.2747′N, 25°7.6929′E) was spudded at 0805 h, using the offset water depth of 521.5 mbrf. A drill-ahead

section was made to 75.3 mbsf. At 1015 h, HLAPC coring recommenced with Cores 2H–6F at 98.8 mbsf, the final depth for Hole U1598B. Excessive torque was again observed, and the decision was made to abandon the hole.

The string was pulled out of the hole with the top drive, and the bit cleared the seafloor at 1430 h. The top drive was racked back, and the pipe trip up continued to 127 mbrf. The bit cleared the rotary table at 1645 h.

The rig floor was secured. The thrusters were raised, starting at 1720 h. The vessel was switched to bridge control at 1725 h. All thrusters were up and secure, and the sea passage started at 1730 h, ending Site U1598.

Table T1. Core summary, Site U1598. mbsf = meters below seafloor. NA = not applicable. DSF = drilling depth below seafloor. H = APC, F = HLAPC, numeric core type = drilled interval. **Download table in CSV format.**

Hole U1598A
Latitude: 36°18.2937′N
Longitude: 25°7.7115′E
Water depth (m): 521.46
Date started (UTC): 1815 h; 24 January 2023
Date finished (UTC): 0515 h; 25 January 2023
Time on hole (days): 0.46
Penetration (mbsf): 79.6
Cored interval (m): 79.6
Recovered length (m): 54.5
Recovery (%): 68.47
Drilled interval (m): NA
Drilled interval (no.): 0
Total cores (no.): 10
APC cores (no.): 8
HLAPC cores (no.): 2

Hole U1598B
Latitude: 36°18.2747′N
Longitude: 25°7.6929′E
Water depth (m): 521.46
Date started (UTC): 0515 h; 25 January 2023
Date finished (UTC): 1530 h; 25 January 2023
Time on hole (days): 0.43
Penetration (mbsf): 98.8
Cored interval (m): 23.5
Recovered length (m): 7.91
Recovery (%): 33.66
Drilled interval (m): 75.3
Drilled interval (no.): 1
Total cores (no.): 5
APC cores (no.): 0
HLAPC cores (no.): 5

Core	Top depth drilled DSF (m)	Bottom depth drilled DSF (m)	Interval advanced (m)	Recovered length (m)	Core recovery (%)	Core on deck date (2023)	Core on deck time UTC (h)
398-U1598A-							
1H	0.0	3.7	3.7	3.74	101	24 Jan	2155
2H	3.7	13.2	9.5	9.61	101	24 Jan	2240
3H	13.2	22.7	9.5	4.32	45	24 Jan	2315
4H	22.7	32.2	9.5	9.72	102	24 Jan	2345
5H	32.2	41.7	9.5	9.84	104	25 Jan	0025
6H	41.7	51.2	9.5	8.37	88	25 Jan	0050
7H	51.2	60.7	9.5	3.54	37	25 Jan	0135
8H	60.7	70.2	9.5	1.49	16	25 Jan	0225
9F	70.2	74.9	4.7	2.36	50	25 Jan	0325
10F	74.9	79.6	4.7	1.51	32	25 Jan	0415
398-U1598B-							
11	0.0	75.3	75.3	****Drilled interval****		25 Jan	0830
2F	75.3	80.0	4.7	1.43	30	25 Jan	0855
3F	80.0	84.7	4.7	1.35	29	25 Jan	0920
4F	84.7	89.4	4.7	1.56	33	25 Jan	0955
5F	89.4	94.1	4.7	1.99	42	25 Jan	1030
6F	94.1	98.8	4.7	1.58	34	25 Jan	1140
		Totals:	178.4	62.41			

3. Lithostratigraphy

Cores from two consecutively drilled holes at Site U1598 (Holes U1598A and U1598B) recovered a stratigraphy from 0 to 95.68 mbsf (Figure F3). Hole U1598A consists of Cores 1H–10F (0–76.41 mbsf), and Hole U1598B includes Cores 2F–6F (75.3–95.68 mbsf).

The recovered material is sedimentary and unlithified in both holes and characterized by dominantly volcanic lithologies (ash/tuff, lapilli-ash, lapilli, and tuffaceous mud/ooze) and lesser nonvolcanic sediments of calcareous mud and ooze (Figures F3, F4). Smear slides for microscopic analyses were prepared to confirm macroscopic descriptions of distinct lithology changes at the section level, such as the identification of vitric ash particles in tuffaceous lithologies or crystals in ash layers. The succession of tuffaceous muds/oozes and volcanic layers defines three subunits (Ia–Ic). X-ray diffraction (XRD) data were obtained from six interstitial water (IW) squeeze cake sediment residues from Hole U1598A.

Figure F3 summarizes the lithostratigraphy of Site U1598, displaying core recovery and the lithostratigraphic unit and subunits in Holes U1598A and U1598B. Table T2 provides the upper and lower boundaries, thicknesses, lithostratigraphic summaries, and biostratigraphic ages of the

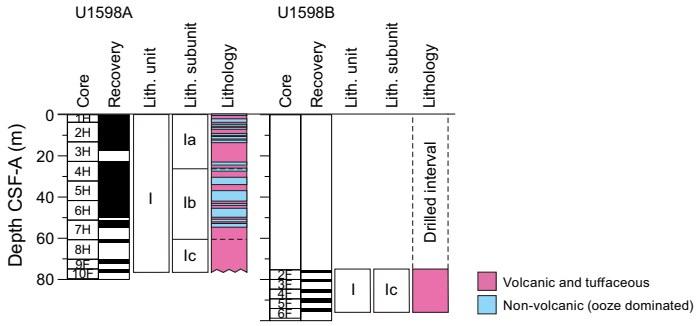

Figure F3. Lithostratigraphic summary, Site U1598. Unit color = dominant lithology.

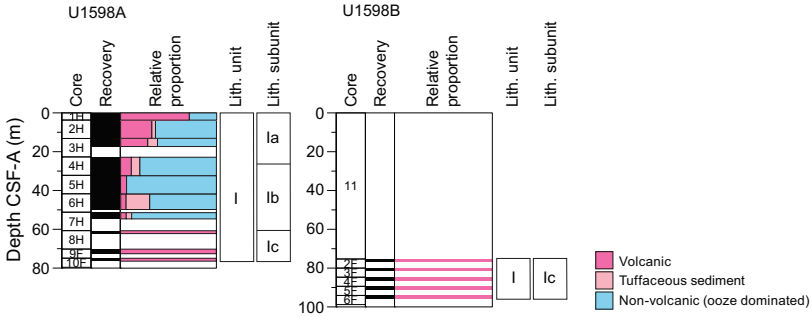

Figure F4. Relative percentages of volcanic, tuffaceous, and nonvolcanic lithologies, Site U1598. Unit I is volcanic rich. Unit I subunits correspond to smaller scale variations of volcanic versus nonvolcanic lithologies.

Table T2. Lithostratigraphic unit and subunits, Site U1598. * = bottom not recovered. † = end of hole. **Download table in CSV format.**

Lith. unit	Subunit	Top depth (mbsf)	Top hole, core, section, interval (cm)	Bottom depth (mbsf)	Bottom hole, core, section, interval (cm)	Thickness (m)	Stratigraphic age	Lithologic summary
			398-		398-			
I	Ia	0.00	U1598A-1H-1, 0	23.96	U1598A-4H-2, 76	24.96	Holocene to mid-Pleistocene	Ash, lapilli-ash, lapilli, tuffaceous mud, and calcareous mud
	Ib	24.96	U1598A-4H-2, 76	54.72*	U1598A-7H-CC, 7	>29.76		Ooze, organic-rich ooze/calcareous mud, tuffaceous mud/ooze, and ash
	Ic	60.70	U1598A-8H-1, 0	76.41*	U1598A-10F-CC, 20†	>15.71		White ash, lapilli, and lesser lithic lapilli
		75.30	U1598B-2F-1, 0	95.68*	U1598B-6F-CC, 25	>20.38	Early Pleistocene?	

lithostratigraphic unit and subunits (see **Biostratigraphy**). Figure **F4** graphically presents the relative proportions of volcanic, tuffaceous, and nonvolcanic lithologies in each hole with the lithostratigraphic unit and subunits. Figure **F5** presents grain size distributions of the sediments, in particular the changes in grain size within the volcanic-dominated subunits, to graphically show the distribution of ash, lapilli-ash, and lapilli. Figure **F6** displays different types of core disturbance observed at Site U1598.

The following sections describe (1) the effects of core disturbance, (2) the lithostratigraphic unit and subunits, and (3) XRD results from Site U1598.

3.1. Core disturbance

Several types of core disturbance disrupt the lithostratigraphy at Site U1598 (Figure **F6**):

- Uparching: slight to moderate coring-induced shear between the sediment and core liner results in bedding uniformly dragged downward along the core margins (Figure **F6A**). In these intervals, original lithofacies and sedimentary structures are usually slightly to severely disturbed but can still be recognized visually.
- Fall-in: usually recognized at the top of cores by coarse clast-supported intervals (Figure **F6B**). We exclude these intervals, which at this site may extend up to 6 cm in thickness, from lithostratigraphy interpretations.
- Mixed sediment: occurs in water-saturated, granular core sections where grains and clasts flow and mix, producing moderately to severely disturbed, partially overprinted, sedimentary structures and stratigraphy (Figure **F6C**).
- Sediment flowage: sediments squeeze out of the formation and flow along the core liner. Relics of squeezed sediments are visible between the liner and the sediment (Figure **F6D**).

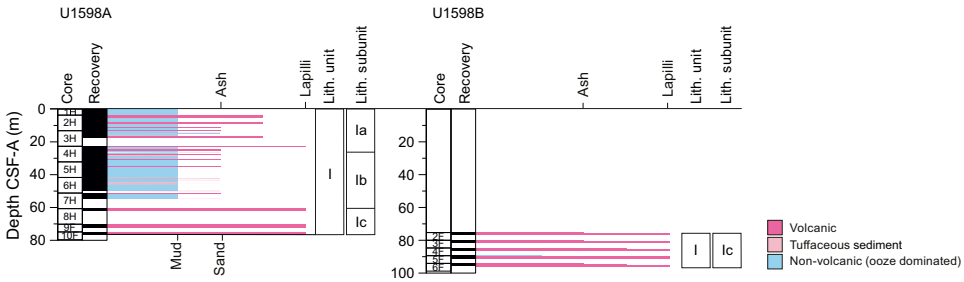

Figure F5. Grain size distributions of volcanics (ash, lapilli-ash, and lapilli), tuffaceous mud, and nonvolcanic sediments, Site U1598. Length of colored bars = relative grain size (ash = <2 mm; lapilli = 2–64 mm; mud = <63 µm; sand = 0.063–2 mm), with separate scales shown for volcanic grain size (top) and nonvolcanic grain size (bottom; used for tuffaceous and nonvolcanic sediments). Mixed lithologies such as lapilli-ash (dark pink) that have relative grain sizes between two categories are plotted between ticks.

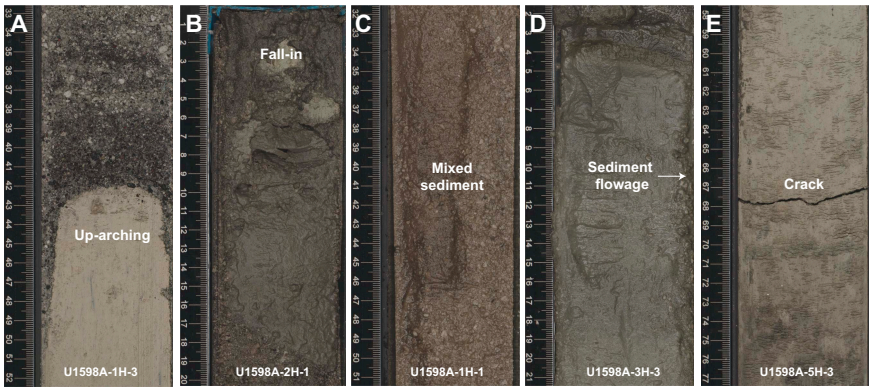

Figure F6. Core disturbances, Site U1598. A. Uparching. B. Fall-in. C. Mixed sediment. D. Sediment flowage. E. Crack.

- Cracks: produced by slight brecciation in the original lithologies (Figure **F6E**).
- Artificial size and density segregation: likely to occur during drilling or with postrecovery core handling processes on board (e.g., inclining, shaking, and plunging cores on the catwalk to compact sediments). Jutzeler et al. (2014) also described pseudohorizontal density grading that can occur while the core is lying flat on deck, resulting in vertical structures once the core is turned upright. Such core disturbance is observed most often in volcanic sediments because increased porosity allows sucking in of seawater during hydraulic piston coring. The resulting soupy texture allows material to flow within the core liner. Secondary normal or reverse grading, or density separation of clasts, may occur as a result of this disturbance and obscure primary sedimentary features.

3.2. Description of unit and subunits

The sediments recovered from Holes U1598A and U1598B comprise one volcanic-rich lithostratigraphic unit (Unit I) (Figure **F3**). Unit I is divided into three subunits (Ia–Ic) (Figures **F4**, **F5**; Table **T2**). The lithology of this unit and subunits is described below.

3.2.1. Unit I

Intervals: 398-U1598A-1H-1, 0 cm, to 10F-CC, 20 cm (bottom of the hole; 76.41 mbsf); 398-U1598B-2F-1, 0 cm, to 6F-CC, 25 cm (bottom of the hole; 95.68 mbsf)
Thickness: >95.68 m
Depth: 0.00–95.68 mbsf
Age: Holocene to Middle Pleistocene
Lithology: volcanic and tuffaceous lithologies (ash, lapilli-ash, and lapilli and tuffaceous mud/ooze) and to a minor extent ooze/organic-rich ooze and organic-rich calcareous mud

Unit I extends from 0 to 76.41 mbsf in Hole U1598A and to 95.68 mbsf in Hole U1598B (Table **T2**). In both holes, coring ended before reaching the bottom of Unit I. Unit I primarily consists of intercalated volcanic and tuffaceous lithologies punctuated by intervals with variable thicknesses of calcareous mud and ooze (Figures **F4**, **F5**). Volcanic intervals (ash, lapilli-ash, and lapilli) commonly have sharp bottom contacts. Figures **F7** and **F8** highlight core section and smear slide images, respectively, of the most common lithologies sampled from Unit I.

Lithologies consisting of >75% volcanic particles (glass shards, pumice, and crystals) comprise ash, lapilli-ash, and lapilli. Description of ash, lapilli-ash, and lapilli in volcanic intervals was based on the relative abundance of ash-sized (<2 mm) and lapilli-sized (2–64 mm) particles, as described in **Lithostratigraphy** in the Expedition 398 methods chapter (Kutterolf et al., 2024), with ash and lapilli used when the proportion of one size was >75% and lapilli-ash used when both sizes were present but at <75% abundance (Fisher and Schmincke, 1984). Macroscopically, ash layers are typ-

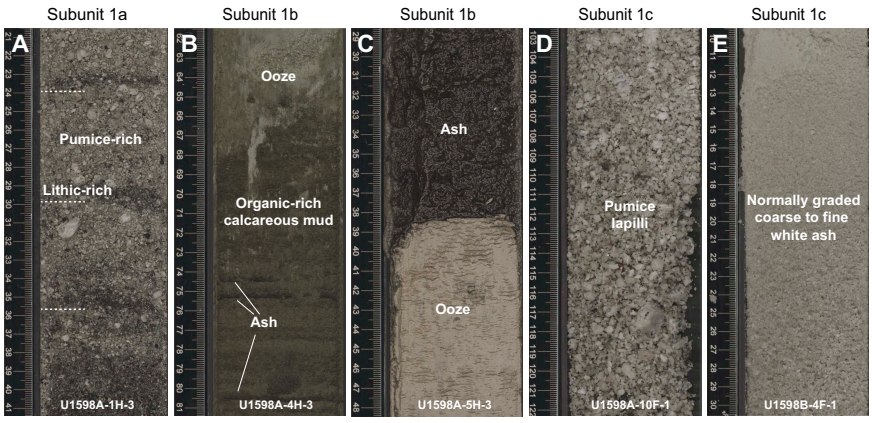

Figure F7. Representative lithologies in Unit I, Site U1598. A. Lapilli-ash with coarser grained pumice-rich and finer grained lithic-rich segregations. B. Ooze and organic-rich calcareous mud with intercalated thin ash layers. C. Ooze overlain by dark gray ash. D. White pumice lapilli. E. Normally graded coarse to fine ash.

ically white to dark gray, well sorted, range in grain size from fine to coarse ash, and variably mixed with mud at the top. Ash layers are typically nongraded or normally graded and are frequently characterized by a sharp base and a more diffuse and often bioturbated upper boundary that grades into tuffaceous mud. Microscopically, ash layers are characterized by colorless to brownish angular glass shards with or without crystals. Some ash layers have distinct crystal/lithic-rich lag deposits at their base (e.g., Sections 398-U1598A-2H-1 and 2H-2). Microscopic observations of smear slides were useful for the identification of specific minerals (e.g., biotite, feldspar, and pyroxene) in ash. The coarser volcanic intervals in Unit I range from monomictic lapilli-ash containing white to gray pumice lapilli with varying proportions of ash matrix to polymictic lithic-vitric lapilli-ash (Figure **F7A**). Where recovered, bottom contacts of these coarser units are sharp or bioturbated but commonly affected by uparching drilling disturbance (Figure **F6A**).

Subunits were defined by the relative proportion of volcanic/tuffaceous intervals and nonvolcanic intervals:

- Subunit Ia (Sections 398-U1598A-1H-1, 0 cm, through 4H-2, 76 cm; 0–23.96 mbsf): primarily lapilli-ash with minor ash and lapilli. Other components include tuffaceous mud/sand, calcareous mud, organic-rich calcareous mud, and minor ooze.
- Subunit Ib (Sections 4H-2, 76 cm, through 7H-CC, 7 cm; 24.96–54.72 mbsf): primarily nonvolcanic material consisting of ooze and organic-rich ooze/calcareous mud, punctuated by tuffaceous mud/ooze and ash.
- Subunit Ic (Sections 8H-1, 0 cm, to the bottom of the hole in Section 10F-CC, 20 cm [60.7–76.41 mbsf], and 398-U1598B-2F-1, 0 cm, to the bottom of the hole in Section 6F-CC, 25 cm [75.3–95.68 mbsf]): ash, lapilli, lapilli-ash, and minor lithic lapilli.

3.2.1.1. Subunit Ia

Subunit Ia extends from 0 to ~23.96 mbsf in Hole U1598A (Sections 1H-1, 0 cm, through 4H-2, 76 cm) (Table **T2**) and is dominated by volcanic and tuffaceous lithologies with up to 0.5 m thick intercalations of fine-grained muds or oozes. Thicknesses of the volcanic intervals vary from 0.05 m to ~3 m, with the thickest packages consisting of lapilli-ashes (Figure **F5**). The uppermost 29 cm of Hole U1598A consists of well-sorted yellowish brown mud that overlies a 2 m thick package of subrounded gray to grayish brown lapilli-ash (Figure **F7A**). This first lapilli-ash is separated from a second lapilli-ash by 0.75 m of calcareous mud and organic-rich calcareous mud. The second lapilli-ash sequence begins with a 10 cm thick ash at 3.76 mbsf that transitions downward into 1.5 m of gray polymictic lapilli-ash interspersed with black ash that contains subrounded gray pumice clasts and volcanic lithics. It has a sharp bottom contact with a light greenish gray calcareous ooze

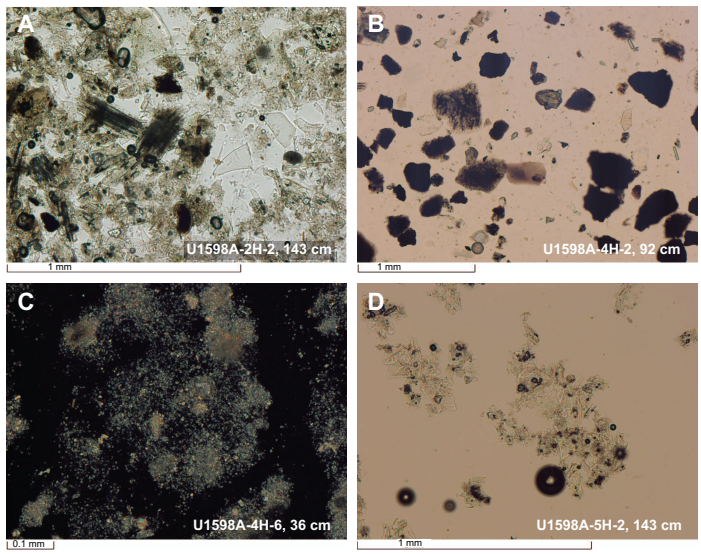

Figure F8. Representative lithologies in Unit I, Site U1598. A. Tuffaceous mud (Subunit Ia). B. Crystal-rich ash (Subunit Ib). C. Crystal-rich tuffaceous ooze (Subunit Ib). D. Ash (Subunit Ib).

at 5.47 mbsf. Below this, organic-rich oozes and calcareous muds are intercalated with gray to black tuffaceous muds (Figure **F8A**), ash, and lapilli-ash (Figure **F5**). Tuffaceous mud contains blocky and pumiceous glass fragments, pyroxene, biotite, feldspar, calcite, and foraminifera (Figure **F8A**). The lowermost lapilli-ash of this subunit is 1.1 m thick and gray and contains pumice and scoria as well as lithics. Subunit Ia ends with a lapilli-bearing ash at 24.96 mbsf.

Similarities in lithology and sedimentary structure can be recognized between this subunit and Subunit Ia at Site U1591 (see **Lithostratigraphy** in the Site U1591 chapter [Druitt et al., 2024b]).

3.2.1.2. Subunit Ib

Subunit Ib begins with a dark grayish brown organic-rich calcareous mud that extends from 24.96 to 54.72 mbsf in Hole U1598A (Sections 4H-2, 76 cm, through 7H-CC, 7 cm). This subunit consists of a package of light greenish gray to olive-gray ooze intercalated with light brownish gray to very dark gray organic-rich (sapropelic) ooze, punctuated by many thin (<10 cm) but discrete dark gray to black ash layers (Figure **F7C, F7D**). Ash layers are characterized by transparent to brownish and blocky glass fragments and may contain numerous crystals (Figure **F8B, F8D**). Some oozes contain ash pods and shell fragments. One 65 cm thick organic-rich (sapropelic) calcareous mud is distinct in that it has multiple intercalated 1–4 cm thick black ash intervals (Figure **F7B**). Figure **F7C** shows the sharp bottom contact of a thicker (60 cm) black ash layer underlain by an ooze. The bottom of Subunit Ib is a 7 cm thick dark gray ash (interval 7H-CC, 0–7 cm).

Similarities in lithology and structure can be recognized between this subunit and Subunit Ib at Site U1591 (see **Lithostratigraphy** in the Site U1591 chapter [Druitt et al., 2024b]).

3.2.1.3. Subunit Ic

Subunit Ic is a coarse volcanic subunit that extends in Hole U1598A from 60.7 mbsf to the bottom of the hole at 76.41 mbsf (Sections 8H-1, 0 cm, through 10F-CC, 20 cm) and in Hole U1598B from 75.3 mbsf to the bottom of the hole at 95.68 mbsf (Sections 2F-1, 0 cm, through 6H-CC, 25 cm). The bottom of Subunit Ic was not recovered in either hole. This subunit consists of multiple normally graded lapilli and lapilli-ash intervals with tens of centimeter-thick lithic-rich intervals at ~75 mbsf in Hole U1598A and ~75 and 80 mbsf in Hole U1598B. The observed normal grading in this subunit could be the result of drilling disturbance and core handling rather than a primary sedimentary feature. The ash and pumice lapilli in this subunit are subrounded to subangular and white or light gray. Rare orthopyroxene was observed at 60–62 mbsf in Hole U1598A, and rare epidote was observed at 80 and 85 mbsf in Hole U1598B. Lithics within this subunit were of volcanic and metamorphic origin.

Similarities in lithology and structure can be recognized between this subunit and Subunit Ic at Site U1591 (see **Lithostratigraphy** in the Site U1591 chapter [Druitt et al., 2024b]).

3.3. X-ray diffraction

XRD data were collected from six IW squeeze cake sediment residues from Hole U1598A. XRD spectra of representative Subunit Ia and Ib lithologies are shown in Figure **F9**. These comprise tuffaceous mud (Figure **F9A**: Section 2H-2; Subunit Ia), calcareous mud (Figure **F9B**: 4H-1; Sub-

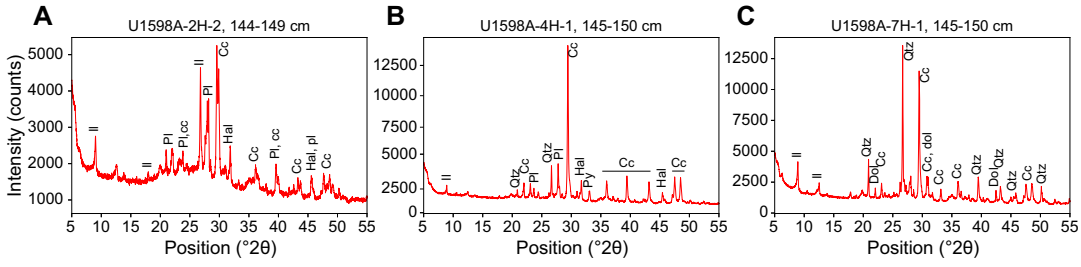

Figure F9. Selected XRD spectra of Subunit Ia and Ib lithologies, Site U1598. A. Tuffaceous mud. B. Calcareous mud. C. Ooze. Il = illite, Pl = Ca-rich plagioclase, Cc = calcium carbonate (calcite, aragonite), Hal = halite, Qtz = quartz, Py = pyrite, Dol = dolomite.

unit Ia), and ooze (Figure **F9C**: 7H-1; Subunit Ib). The tuffaceous mud shows the characteristic amorphous hump at low °2θ, indicating the presence of volcanic glass. Identified minerals in all three lithologies are calcium carbonate (calcite, aragonite), quartz, and clay minerals of the illite group. In addition, typically Ca-rich plagioclase, dolomite, halite, and pyrite were identified in some of these lithologies.

4. Stratigraphic correlation

Two holes were drilled at Site U1598. Hole U1598A was drilled to 76.41 mbsf using the APC and HLAPC systems (APC: 0–62.19 mbsf; HLAPC: 70.2–76.41 mbsf). Hole U1598B was drilled without recovery to 75.3 mbsf and then cored to 95.68 mbsf using the HLAPC system. Both holes had only a short overlap between 75.3 and 76.41 mbsf, and no reliable correlation could be identified. Therefore, no affine ties were generated and no shifts were applied to the cores. To illustrate this, Figure **F10** shows the magnetic susceptibility (MS), natural gamma radiation (NGR), and gamma ray attenuation (GRA) density measurements from Holes U1598A and U1598B together (see **Physical properties**), along with the respective depth of the cores.

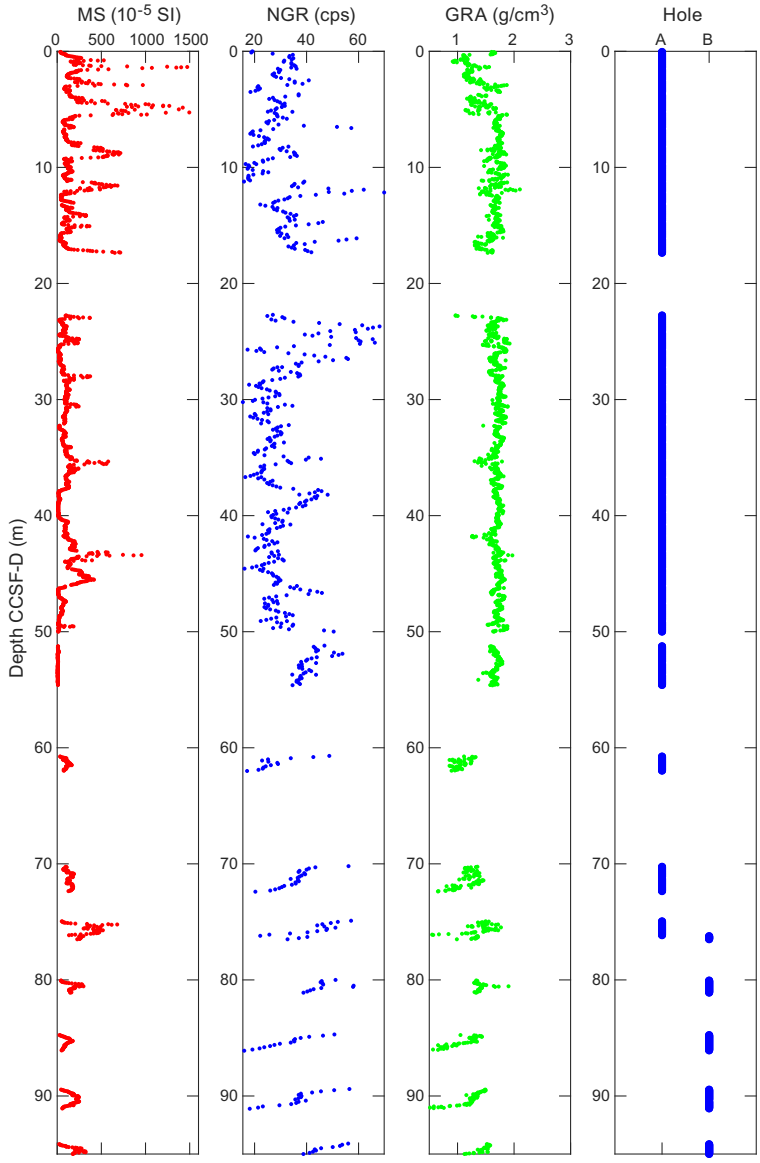

Figure F10. MS, NGR, and GRA density, Site U1598. For WRMSL data, see Physical properties.

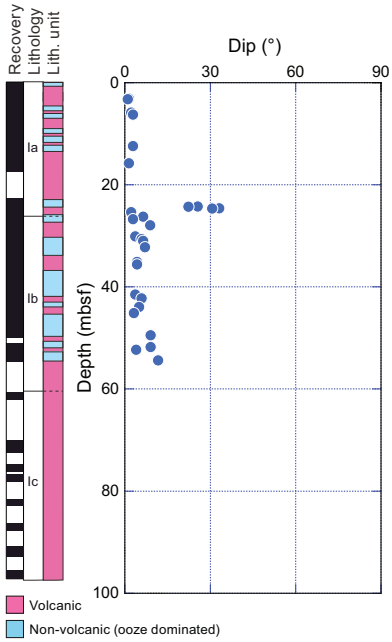

Figure F11. Dip data, Site U1598.

5. Structural geology

Structural geology analyses at Site U1598 included description of cores retrieved from Hole U1598A. A total of 28 bedding structures were measured, mostly from relatively consolidated intervals. The distributions and dip angles of planar structures (measured to an estimated accuracy of ±2°) are shown in Figure **F11**. Bedding planes were measured mainly on thin sand beds/laminae and mud boundaries and mostly exhibit horizontal to subhorizontal dips ranging 1°–12° (mean = 5°). However, steeper inclinations develop in slumps in the depth interval 24–25 mbsf at the bottom of Lithostratigraphic Subunit Ia, where dips range 22°–33° (mean = 28°) (Figure **F11**). Deformation related to drilling and core recovery was noted but not recorded.

6. Biostratigraphy

Planktonic foraminifera, benthic foraminifera, and calcareous nannofossils were examined from core catcher samples and additional split core samples from Hole U1598A to develop a shipboard biostratigraphic framework for Site U1598. Additionally, planktonic and benthic foraminifera provided data on paleowater depths, downslope reworking, and possible dissolution.

Site U1598 cored the Christiana Basin sedimentary sequence and recovered a 76.41 m thick Holocene to Middle Pleistocene sequence composed primarily of volcanogenic sediments and calcareous and tuffaceous oozes. Calcareous nannofossils and planktonic foraminifera provided good resolution in the Holocene through Pleistocene sediments. Biostratigraphic datums recognized at Site U1598 are given in Tables **T3** and **T4**, and an age-depth plot is shown in Figure **F12**.

Hole U1598A recovered Holocene to Middle Pleistocene–aged sediments (0–0.51 Ma) from Samples 1H-CC, 12–19 cm, to 6H-CC, 0–2 cm (3.74–50.07 mbsf), and sediments of indeterminate age from Samples 7H-CC, 7–9 cm, to 10H-CC, 0–5 cm (54.74–76.41 mbsf).

6.1. Calcareous nannofossils

Calcareous nannofossil biostratigraphy in Hole U1598A was established through analysis of core catcher samples. Nannofossils are common to very rare in samples from the Pleistocene sequence (3.71–54.73 mbsf). Preservation is moderate to poor throughout the sequence, and there is signif-

icant reworking of older material in most of the Pleistocene samples. Two nannofossil biostratigraphic datums are recognized at Site U1598, representing a continuous Pleistocene sedimentary sequence. Biostratigraphic datums are given in Table **T3**, and distribution of calcareous nannofossil taxa is shown in Table **T5**.

The presence of *Emiliania huxleyi* in Samples 398-U1598A-1H-CC, 10–12 cm, and 2H-CC, 0–3 cm (3.705–13.115 mbsf), indicates a Middle Pleistocene to Holocene age (≤0.265 Ma) within Zones MNN21a and MNN21b (CNPL11: Backman et al., 2012; NN21: Martini, 1971; CN15: Okada and Bukry, 1980) of Rio et al. (1990) and Di Stefano and Sturiale (2010) (Figure **F13**). The last appearance datum of *Pseudoemiliania lacunosa* defines the Zone NN19/20 boundary. The last consistent appearance of *P. lacunosa* in Hole U1598A occurs in Sample 5H-CC, 28–30 cm (42.03 mbsf).

6.2. Foraminifera

Planktonic and benthic foraminifera were examined from core catcher samples and split core samples from Hole U1598A (Figure **F12**). Absolute ages assigned to biostratigraphic datums follow those listed in Table **T4**. Planktonic foraminifer datums are given in Table **T3**; the distribution of important planktonic and benthic foraminifer taxa is given in Tables **T6** and **T7**; and planktonic

Table T3. Calcareous nannofossil events and absolute ages, Site U1598. **Download table in CSV format.**

Calcareous nannofossil event	Age (Ma)	Top core, section, interval (cm)	Bottom core, section, interval (cm)	Top depth CSF-A (m)	Mid-depth CSF-A (m)	Bottom depth CSF-A (m)
		398-U1598A-	398-U1598A-			
Base of *Emiliania huxleyi*	0.265	2H-CC, 0–3	3H-CC, 10–12	13.13	15.315	17.50
Top of *Pseudoemiliania lacunosa*	0.467	4H-CC, 25–29	5H-CC, 28–30	32.42	37.22	42.02

Table T4. Foraminiferal events and absolute ages, Site U1598. **Download table in CSV format.**

Foraminifer events	Age (Ma)	Top core, section, interval (cm)	Bottom core, section, interval (cm)	Top depth CSF-A (m)	Mid-depth CSF-A (m)	Bottom depth CSF-A (m)
		398-U1598A-	398-U1598A-			
Base common *Truncorotalia truncatulinoides*	0.53	4H-CC, 25–29	5H-CC, 28–30	32.42	37.22	42.02

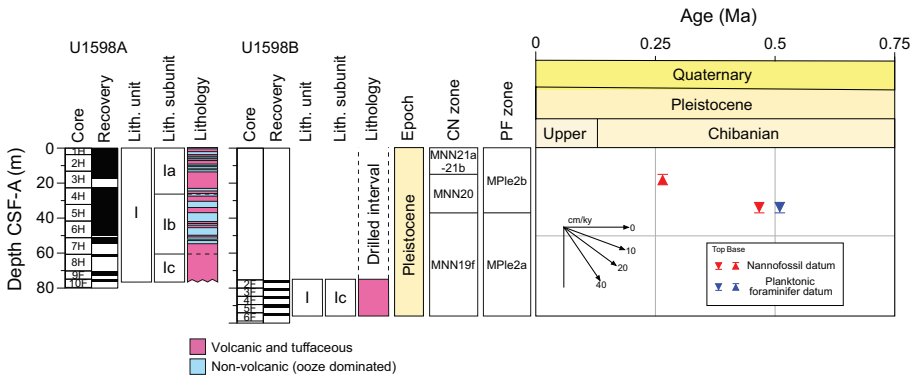

Figure F12. Age-depth plot, Hole U1598A. Integrated biochronology is shown. CN = calcareous nannofossil. PF = planktonic foraminifer. Biohorizons correspond to those given in Tables T3 and T4. Biohorizons denoted with a question mark are not fully constrained and are interpolated.

Table T5. Distribution of calcareous nannofossils, Site U1598. **Download table in CSV format.**

foraminifer abundances and indications of oceanicity (Hayward et al., 1999), paleowater depths, and downslope reworking are shown in Figures **F14** and **F15**.

Because of the volcanogenic nature of the cored sedimentary sequence, residues (>125 µm) from washed samples were often significantly composed of volcaniclastic particles such as pumice, scoria, and ash that diluted the microfossil component of residues. Foraminifera dominated the

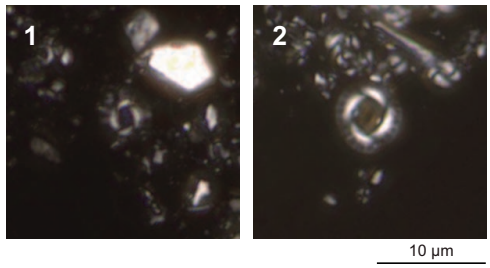

Figure F13. Calcareous nannofossils, Hole U1598A. 1. *Emiliania huxleyi* (Lohmann) Hay and Mohler (1H-CC, 12–19 cm). 2. *Pseudoemiliania lacunosa* (Kamptner) Gartner (5H-CC, 28–30 cm).

Table T6. Distribution of planktonic foraminifera, Site U1598. **Download table in CSV format.**

Table T7. Distribution of benthic foraminifera, Site U1598. **Download table in CSV format.**

Core, section, interval (cm)	Bottom depth CSF-A (m)	Abundance	Preservation	OK Planktonic (%)	AW Planktonic (%)	Planktonic mean (%)	Zone	Age (Ma)	Oceanicity	Paleowater depth (m)
398-U1598A-										
1H-CC	3.74	C	G	58	53	55.5		<0.51	Extra-neritic	300-700
2H-CC	13.13	R	VG-M	54	68	61		<0.51	Sub-oceanic	
3H-CC	17.52	R	VG	83	81	82	MPle2b	<0.51		NA
4H-CC	32.42	A	G-M	90	93	91.5		<0.51	Oceanic	
5H-CC	42.04	C	G-M	65	65	65		<0.51	Sub-oceanic	300-700
6H-CC	50.07	R	G	79	91	85	MPle2a	>0.51		NA
7H-CC	54.74	R	VG	69	85	77	Contamination	Contamination		

Figure F14. Foraminiferal oceanicity and paleowater depth estimates, Site U1598. Blue colors show relationship between oceanicity index and paleowater depth. Observers: OK = Olga Koukousioura, AW = Adam Woodhouse. NA = not applicable.

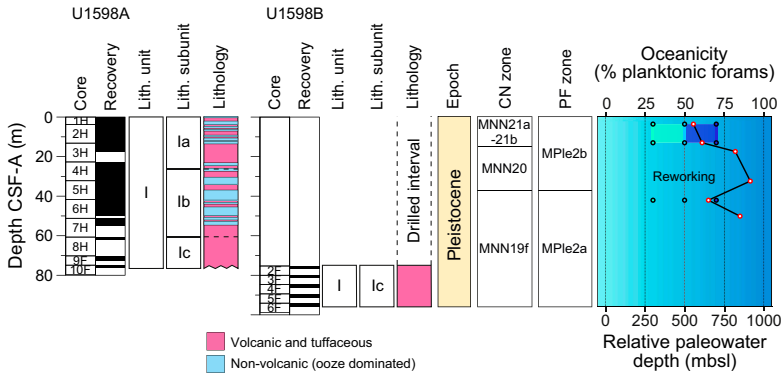

Figure F15. Biostratigraphic summary, Site U1598. CN = calcareous nannofossil, PF = planktonic foraminifer. Interpreted oceanicity: solid line/red points = interpreted oceanicity, dashed line = extrapolation through barren/unreliable sample data. Interpreted paleowater depths: light blue points/shading = shallower paleowater depths, dark blue points/shading = deeper paleowater depths.

biogenic component of residues, however. Additionally, volcanic material, clastic grains, minor pyrite, carbonaceous plant-derived matter, and other fossil material, including shells and fragments (Bivalvia and Gastropoda), Pteropoda, Scaphopoda, Bryozoa, Arthropoda (crab claws), echinoid spines and plate fragments, and radiolarians, as well as ostracods, were also present in variable amounts in most samples.

In the Holocene to Middle Pleistocene section, foraminifera with very good to moderate preservation are present in siliciclastic and volcaniclastic sediments. Foraminifer abundances are also variable and are notably rare in tuffaceous oozes, likely due to sedimentary dilution, whereas coarser volcaniclastic intervals are sometimes barren.

6.2.1. Holocene to Early Pleistocene biostratigraphy

Because of explosive volcanic events and rapid deposition of the upper sedimentary section, the base of the Holocene is not possible to assign accurately. Planktonic foraminifer assemblages from the Holocene to Early Pleistocene section of Site U1598 are mostly very well preserved where specimens are rarely broken or exhibiting partially dissolved shell walls.

Holocene to Pleistocene foraminifer faunas suggest moderate fluctuations in relative paleowater depth and oceanicity with variable planktonic abundances that range 56%–92% where foraminifera are present (Figure **F15**). The fauna are typical of Pleistocene Mediterranean biostratigraphic zones, primarily composed of *Neogloboquadrina incompta*, *Globigerina bulloides*, *Globigerinita glutinata*, *Globigerinoides elongatus*, *Globigerinoides pyramidalis*, *Globigerinoides ruber* var. white, *Globoconella inflata*, *Hirsutella scitula*, *Neogloboquadrina pachyderma*, *Orbulina universa*, *Turborotalita quinqueloba*, and *Globigerinella calida* (Figure **F16**).

Foraminiferal faunas are sufficiently common to biostratigraphically divide the Pleistocene into two Mediterranean planktonic foraminiferal biostratigraphic zones (Lirer et al., 2019):

- Zone MPle2b (0.00–0.53 Ma): 3.74–32.42 mbsf.
- Zone MPle2a (0.53–0.94 Ma): 42.04–50.07 mbsf.

Because of potential downhole contamination, samples located deeper than 50.07 mbsf were not assigned to a biostratigraphic zone. The faunal criteria on which these age assignments are based are given below.

6.2.1.1. Zone MPle2b (0.00–0.53 Ma)

Samples 398-U1598A-1H-CC, 12–19 cm, to 4H-CC, 25–29 cm (3.74–32.42 mbsf), are assigned to Zone MPle2b based on the first occurrence of *Truncorotalia truncatulinoides* (first common

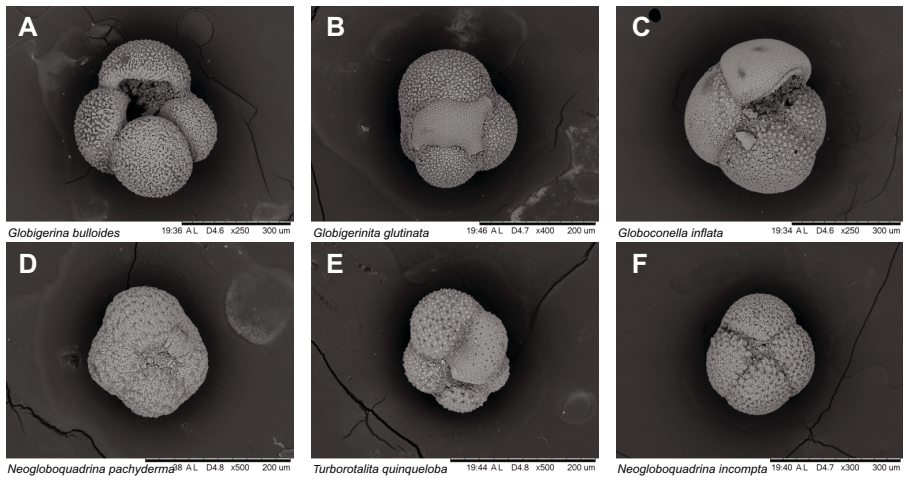

Figure F16. Planktonic foraminifera, Sample 398-U1598A-2H-CC, 0–3 cm. A. *Globigerina bulloides*. B. *Globigerinita glutinata*. C. *Globoconella inflata*. D. *Neogloboquadrina pachyderma*. E. *Turborotalita quinqueloba*. F. *Neogloboquadrina incompta*.

occurrence = 0.53 Ma), which is generally rare in the Aegean Sea, likely due to the shallow water depths (Lirer et al., 2019).

6.2.1.2. Zone MPle2a (0.53–0.94 Ma)

Samples 398-U1598A-5H-CC, 28–30 cm, to 6H-CC, 7–9 cm (42.04–50.07 mbsf), are assigned to Zone MPle2a based on the absence of *T. truncatulinoides* s.l. (0.53–0.934 Ma) and the sporadic occurrences of sinistrally coiled *Neogloboquadrina* spp. (0.51–0.91 Ma) throughout this interval.

6.2.2. Planktonic foraminiferal oceanicity

Planktonic foraminifer abundances are relatively variable, ranging 56%–92% where foraminifera are present (Figure **F15**). Oceanicity values are generally in agreement with benthic foraminiferal paleowater depth indicators in intervals where reworking is low or absent. The oceanicity data for Site U1598 generally indicate fluctuations from extraneritic to oceanic conditions (100 to >1000 mbsl) through the study section, with a slight trend of deepening paleowater downcore (Figure **F15**).

6.2.3. Benthic foraminifera paleowater depths

Benthic foraminiferal assemblages are highly variable between abundant to very rare with common reworked/transported specimens. The low abundances of benthic foraminiferal faunas in most samples, such as Samples 398-U1598A-3H-CC, 10–12 cm, to 4H-CC, 25-29 cm (17.52–32.42 mbsf), and 6H-CC, 0–2 cm, to 7H-CC, 7–9 cm (50.07–54.74 mbsf), are possibly correlated with rapid emplacement of volcaniclastic sediments and/or inhospitable environmental conditions. Consequently, no paleowater depth estimates were possible for these intervals. The benthic foraminifer distributions indicate uppermost to upper bathyal (300–700 mbsl) paleowater depths (Figure **F15**) for Samples 1H-CC, 12–19 cm, to 2H-CC, 0–3 cm (3.74–13.13 mbsf), and 5H-CC, 28–30 cm (42.04 mbsf), which contain common and rare benthic foraminifera of the upper bathyal species *Cassidulina* spp., *Cibicidoides crebbsi*, *Gyroidina* spp., and *Trifarina angulosa*, as well as other shelf to bathyal markers including common *Uvigerina peregrina* and common uppermost bathyal species such as *Bolivina spathulata*. Finally, samples in various intervals exhibit broken and mixed reworked foraminifer faunas, which in some cases are highly abundant, such as in Sample 4H-CC, 25–29 cm (32.42 mbsf), most likely representing downslope reworking and sediment transportation (Figure **F15**).

7. Paleomagnetism

A total of 30 archive-half sections recovered from Hole U1598A were suitable for paleomagnetic analysis using the 2G Enterprise superconducting rock magnetometer (SRM) system. Alternating field (AF) demagnetization of these sections yielded a total of 1592 measurements in the sections and shows magnetizations generally decayed linearly to the origin following removal of a low-coercivity drilling-induced component after demagnetization at 15 mT (Figure **F17**). The mean inclination of principal component directions that passed the statistical filtering described for Site U1591 (see **Paleomagnetism** in the Site U1591 chapter [Druitt et al., 2024b]) is +51.6° (k = 72.9; α_{95} = 0.6; n = 1306). This is slightly shallower than the geocentric axial dipole field inclination of +56° at this site (Figure **F17**). Eight discrete samples were also AF demagnetized, and all showed normal polarities of magnetization. No reversals are present in the data set, and the sampled interval is therefore assigned to the Brunhes Chron (C1n, <0.773 Ma; Gradstein et al., 2020), which is compatible with available biostratigraphic age constraints (see **Biostratigraphy**).

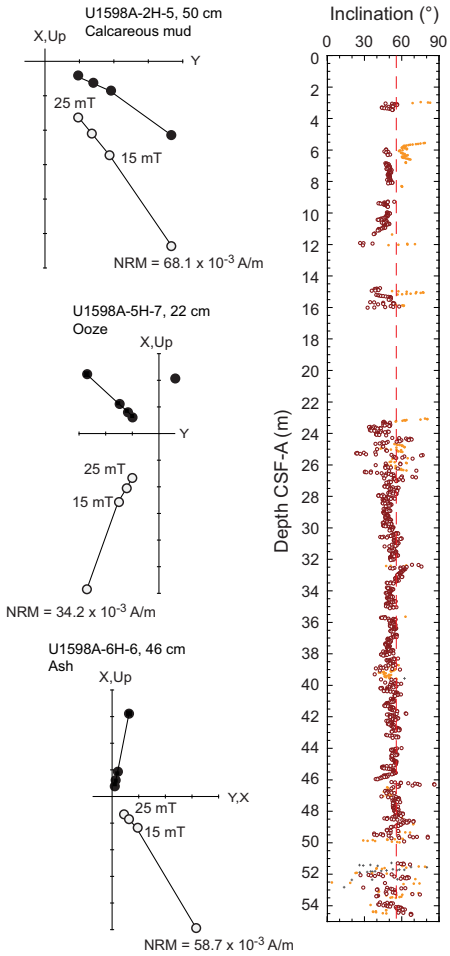

Figure F17. Left: AF demagnetization of archive-half sections, Hole U1598A. Solid circles = projection onto horizontal plane, open circles = projection onto vertical plane. NRM = natural remanent magnetization. Right: archive-half section magnetic inclinations, Hole U1598A. Open symbols = principal component analysis inclinations from 15–25 mT demagnetization, solid symbols = Fisher mean inclinations from 15–25 mT demagnetization, crosses = inclinations after 25 mT demagnetization. Red dashed line = geocentric axial dipole inclinations expected at this site.

8. Physical properties

The typical increases of bulk density, *P*-wave velocity, and thermal conductivity with increasing depth are not clearly documented at Site U1598. MS is highly variable in volcaniclastic layers and is sometimes very high. Grain density in volcanic lapilli layers is sometimes <2.0 g/cm^3.

8.1. Whole-round GRA density, MS, *P*-wave velocity, and NGR

Figure F18 summarizes data collected on whole-round cores measured on the GRA densitometer, MS loop, and *P*-wave logger on the Whole-Round Multisensor Logger (WRMSL), as well as NGR. All cited depths are on the CSF-A scale. A few possible systematic sources of error in these data should be considered when interpreting absolute values and trends:

- Redistribution of unconsolidated volcaniclastic materials in core liners during coring and on the core receiving platform can lead to sorting by particle size and density.
- Core liners often contained large amounts of water. As a result, WRMSL measurements of bulk density are systematically lower than discrete measurements at this site.
- Whole-round measurements in sections that match discrete measurement values on split cores are most reliable.

The volcanic lapilli of Lithostratigraphic Subunit Ic have distinctly lower density than the nonvolcanic, ooze-dominated lithologies of Subunits Ia and Ib. MS is highly variable within the volcaniclastic deposits at this site and can be very high (>2500 × 10^{-5} SI). High values of MS correspond to volcaniclastic layers. Two high *P*-wave velocity layers, one around 5 mbsf and the other at about 71 mbsf, correspond to lapilli-ash layers in Hole U1598A.

Overall, there is no clear systematic increase in bulk density and *P*-wave velocity with increasing depth. Whether the lack of a signature of compaction is real, a consequence of the limited depth of the holes, or an artifact of drilling and recovery disturbances cannot be readily determined.

8.2. Discrete measurements

8.2.1. Material strength

Sediment strength was measured using a pocket penetrometer (PP) on the catwalk immediately after section splitting. Automated vane shear (AVS) strength measurements were made on working-half sections. Only Hole U1598A samples were suitable for strength measurements. A total of seven AVS measurements were made on working-half sections in Hole U1598A (Figure **F19**; Table **T8**). A total of six PP measurements were made on fine-grained materials that remained intact in core liners upon recovery on the catwalk (Table **T8**).

8.2.2. *P*-wave velocity

Totals of 200 and 9 discrete *P*-wave velocity measurements were conducted on Hole U1598A and U1598B working-half sections, respectively (Figure **F19**; Table **T9**). *P*-wave velocity ranges 1.50–2.45 km/s (mean = 1.61 km/s). Discrete measurements of *P*-wave velocity on working-half core sections are similar to those measured using WRMSL on whole-round cores (Figure **F18**).

Discrete measurements were sometimes challenging to make in coarse, pumice-rich deposits because signals were especially noisy. Furthermore, the particle size was a substantial fraction of the distance between the two calipers used to make the measurements; hence, the measurements may not be representative of true bulk properties (i.e., sample size is not much larger than a representative elementary volume).

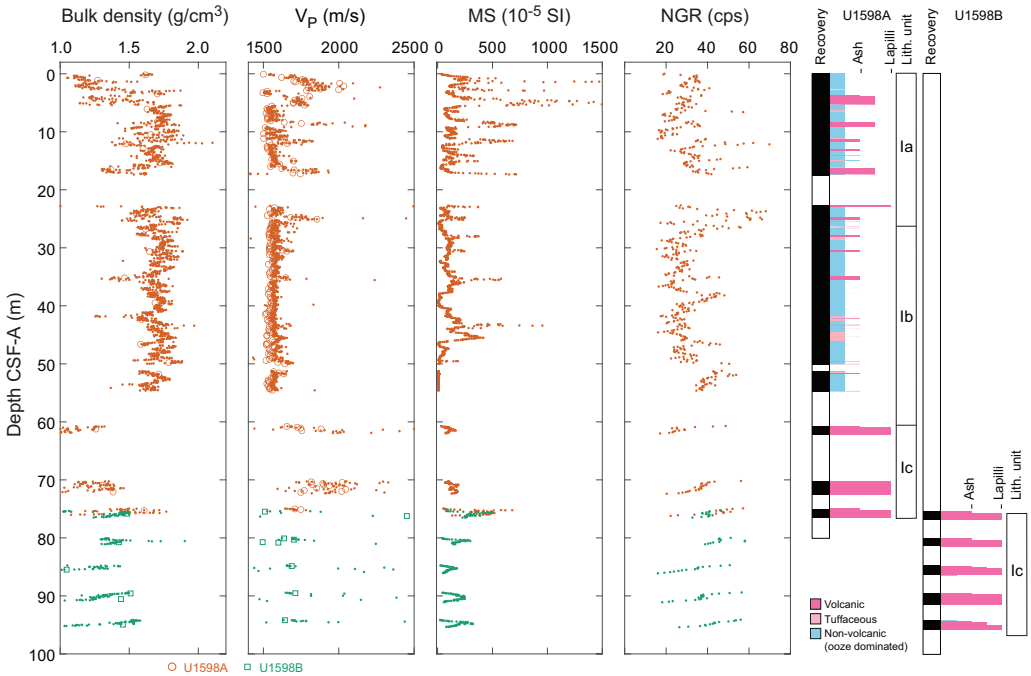

Figure F18. Physical properties, Site U1598. Dots = whole-round measurements, open symbols = discrete measurements. Note that MS values > 1500 × 10^{-5} SI are not shown. cps = counts per second.

8.2.3. Moisture and density

Totals of 26 and 6 discrete samples were collected from Holes U1598A and U1598B, respectively, to conduct moisture and density (MAD) measurements (Figure **F19**; Table **T10**). Bulk density derived using MAD measurements on discrete samples should be more reliable than GRA density data from WRMSL measurements on whole-round cores, although in both cases coring and recovery disturbances may have impacted measured values.

Porosity ranges 50–74 vol% (mean = 63 vol%; standard deviation = 6 vol%). Bulk density ranges 1.05–1.79 g/cm^3 (mean = 1.54 g/cm^3). Bulk density is lower in volcaniclastic materials than ooze-dominated sediment.

Grain density ranges 1.10–2.79 g/cm^3 (mean = 2.41 g/cm^3; median = 2.62 g/cm^3). The lowest values occur in volcaniclastic subunits. Most of the low grain densities are found in lapilli layers deeper than 60 mbsf.

8.2.4. Thermal conductivity

A total of seven thermal conductivity measurements were made on selected working-half sections (Table **T11**). Measurements could not be made on coarse volcaniclastic materials; hence, the values we report are not representative of the full range of recovered lithologies. No measurements were possible in Hole U1598B. The mean thermal conductivity is 1.06 W/(m·K). There is no apparent increase in thermal conductivity with increasing depth (Figure **F19**).

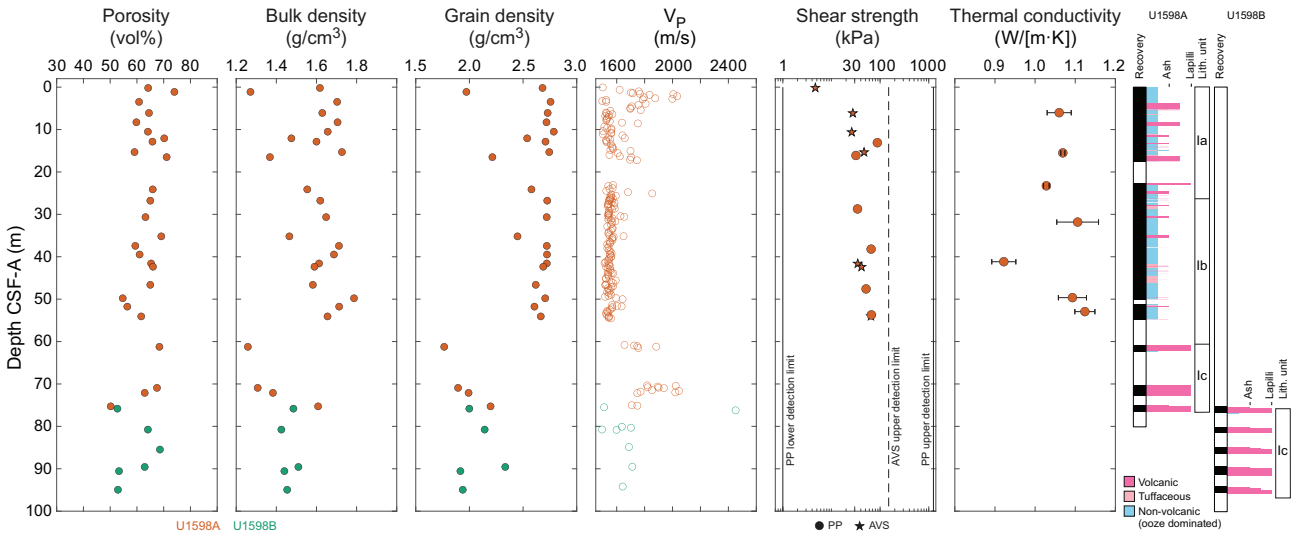

Figure F19. Discrete physical properties measurements, Site U1598. Dashed line = AVS upper measurement limit, solid lines = PP measurement limits.

Table T8. Shear strength, Site U1598. **Download table in CSV format.**

Table T9. *P*-wave velocity, Site U1598. **Download table in CSV format.**

Table T10. MAD measurements, Site U1598. **Download table in CSV format.**

Table T11. Thermal conductivity, Site U1598. **Download table in CSV format.**

9. Geochemistry

9.1. Volcaniclastic bulk geochemistry

To determine the geochemistry of the volcanic and tuffaceous materials, one tephra sample was handpicked from Hole U1598A. Following cleaning, grinding, fusion, and dissolution, the material was analyzed shipboard for major (Si, Al, Fe, Mg, and Ca), minor (Ti, Mn, Na, K, and P), and trace (Sc, V, Cr, Co, Ni, Cu, Zn, Rb, Sr, Y, Zr, Nb, Ba, Ce, and Nd) elements using inductively coupled plasma–atomic emission spectroscopy (ICP-AES) (see **Geochemistry** in the Expedition 398 methods chapter [Kutterolf et al., 2024]). The sample was run multiple times to determine analytical reproducibility.

9.1.1. ICP-AES: major, minor, and trace elements

The volcaniclastic unit sampled was classified as a dacite (Table **T12**; Figure **F20**). Bulk chemistry values are less evolved than glass chemistry reported in Kutterolf et al. (2021), as expected due to bulk analyses including both minerals and glass.

Concentrations are reported for all analyzed trace elements, but Ce, Cr, Cu, Nb, Ni, P, Rb, S, and V were below detection limits and are not shown in Table **T12**; volcaniclastic analytical errors are ±1% for major elements and ±5%–10% for trace elements (see **Geochemistry** in the Expedition 398 methods chapter [Kutterolf et al., 2024]). Trace element ratios were used to broadly discriminate between the volcanic centers of Kolumbo, Santorini, and Christiana.

9.2. Interstitial water geochemistry

To determine the inorganic constituents of IW, a total of seven water samples were taken from the mudline and whole-round squeezing of sediment intervals at Site U1598. Aliquots of IW were used for shipboard analyses, and the remaining water was taken for shore-based analysis following protocols specified by individual scientists. The retrieved pore waters were analyzed shipboard for

Table T12. ICP-AES data for major, minor, and trace elements, Site U1598. **Download table in CSV format.**

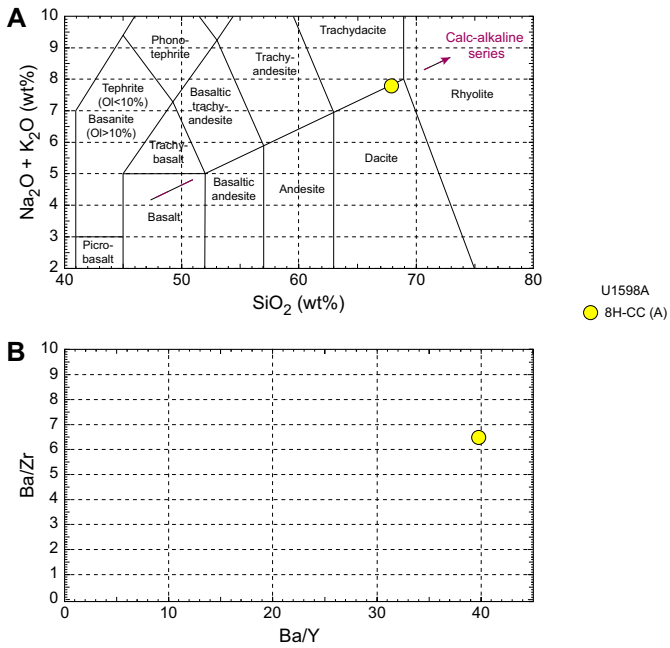

Figure F20. ICP-AES analyses of selected volcaniclastic units used to discriminate between potential volcanic sources, Site U1598. A. Total alkali vs. SiO_2 plot with the rock nomenclature of Le Maitre et al. (2002) overlain used for sample naming. Ol = olivine. B. Ba/Y vs. Ba/Zr plot used to correlate samples.

salinity, alkalinity, pH, major anions (Cl^-, SO_4^{2-}, and Br^-), major cations (Ca^{2+}, Na^+, Mg^{2+}, and K^+), and major (S, Ca, Mg, K, and Na) and minor (B, Ba, Fe, Li, Mn, P, Si, and Sr) elements using the methods described in **Geochemistry** in the Expedition 398 methods chapter (Kutterolf et al., 2024).

9.2.1. Salinity, alkalinity, and pH

Salinity ranges 40–70, with the maximum occurring at 33.7 mbsf before salinity decreases to the base of the hole (Table **T13**; Figure **F21**).

Total alkalinity increases (2.5–6.8 mM) with depth to 14.7 mbsf before decreasing to the base of the hole at 52.7 mbsf (Table **T13**; Figure **F21**).

Values for pH show slight variation within the sampled depths, ranging 7.3–7.8 (average = 7.5 ± 0.3) (Table **T13**; Figure **F21**). The maximum value is at the mudline, and IW samples cluster between pH values of 7.3 and 7.4.

9.2.2. Bromide, chloride, boron, sodium, potassium, magnesium, calcium, and sulfate

Similar to other sites, Br^-, Cl^- B, Na^+, K^+, Mg^{2+}, Ca^{2+}, and SO_4^{2-} trends resemble trends in salinity (Table **T14**; Figure **F22**). Maxima are reached at 24.2 mbsf in B, Ca^{2+}, and K^+, whereas Br^-, Cl^-, Na^+, Mg^{2+}, and SO_4^{2-} maxima are at 33.7 mbsf, matching the maximum salinity value. All values decrease to the base of the hole below 33.7 mbsf.

9.2.3. Lithium, iron, manganese, barium, silicon, and strontium

Trends for Li, Mn, Ba, Si, and Sr do not follow salinity, as above (Table **T14**; Figure **F23**). Lithium concentrations increase to a maximum of 173 µM at 24.2 mbsf and decrease below that depth. Strontium increases with depth and reaches its highest concentration near the bottom of Hole U1598A at 46 mbsf. Iron and Mn concentrations are elevated in the uppermost 35 m and generally decrease downhole. Concentrations of Ba show little variation other than one elevated value of 2.8 µM at 46 mbsf. IW Si concentrations increase to a maximum of 775 µM at 14.7 mbsf. Silicon is elevated in the lowermost two samples, increasing with depth. Phosphorus was below the detection limit in all samples and is therefore not plotted.

Table T13. Alkalinity, pH, and salinity values, Site U1598. **Download table in CSV format.**

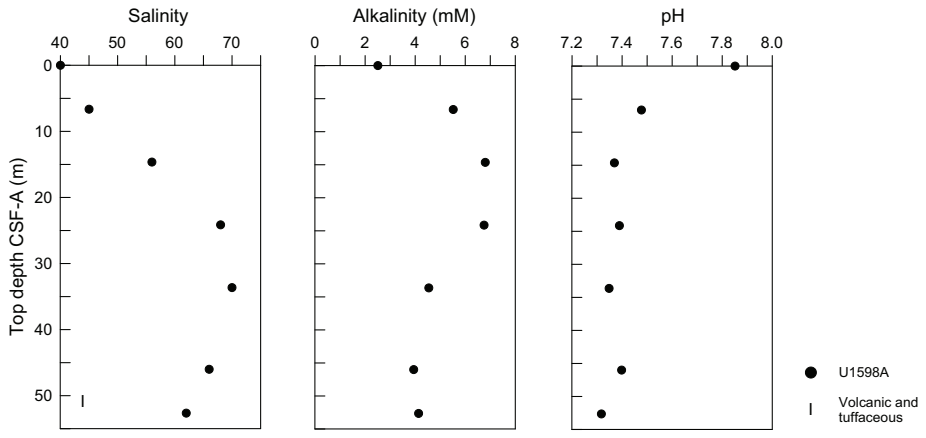

Figure F21. IW salinity, alkalinity, and pH, Site U1598. Lithostratigraphic Unit I is described in Lithostratigraphy.

Table T14. IW data for major anions and cations measured using ion chromatography and major and minor elements measured using ICP-AES, Site U1598. **Download table in CSV format.**

9.3. Sediment bulk geochemistry

Six sediment samples were analyzed for bulk geochemistry (Table **T15**). All were analyzed for total carbon, hydrogen, and nitrogen (CHN) and for inorganic carbon and carbonate content following the protocols explained in **Geochemistry** in the Expedition 398 methods chapter (Kutterolf et al., 2024). For CHN analysis, duplicates were run for ~10% of the samples to determine analytical reproducibility (standard deviations: N = 0.01; C = 0.04). Carbonate values range 21–42 wt% (Figure **F24**).

9.3.1. Sapropel identification

Total organic carbon (TOC) was calculated using total carbon and inorganic carbon values. Following the convention set forth by Kidd et al. (1978), units with TOC values >2.0 wt% were identified as sapropels and units with TOC values of 0.5–2.0 wt% were identified as sapropelitic. Using these values, three units were identified as sapropelitic and one unit was identified as a sapropel at 24 mbsf (Figure **F24**).

9.4. Headspace gas analysis

Headspace gas analyses were performed at a resolution of one sample per full-length core (9.5 m advance) throughout Hole U1598A. The aim was to monitor the presence and abundance of C_1–C_3 hydrocarbons as part of the standard International Ocean Discovery Program safety protocol (Pimmel and Claypool, 2001). A total of nine headspace gas samples from this hole were analyzed using gas chromatography (see **Geochemistry** in the Expedition 398 methods chapter [Kutterolf et al., 2024]). Methane, ethane, and propane concentrations were below the detection limit throughout Hole U1598A.

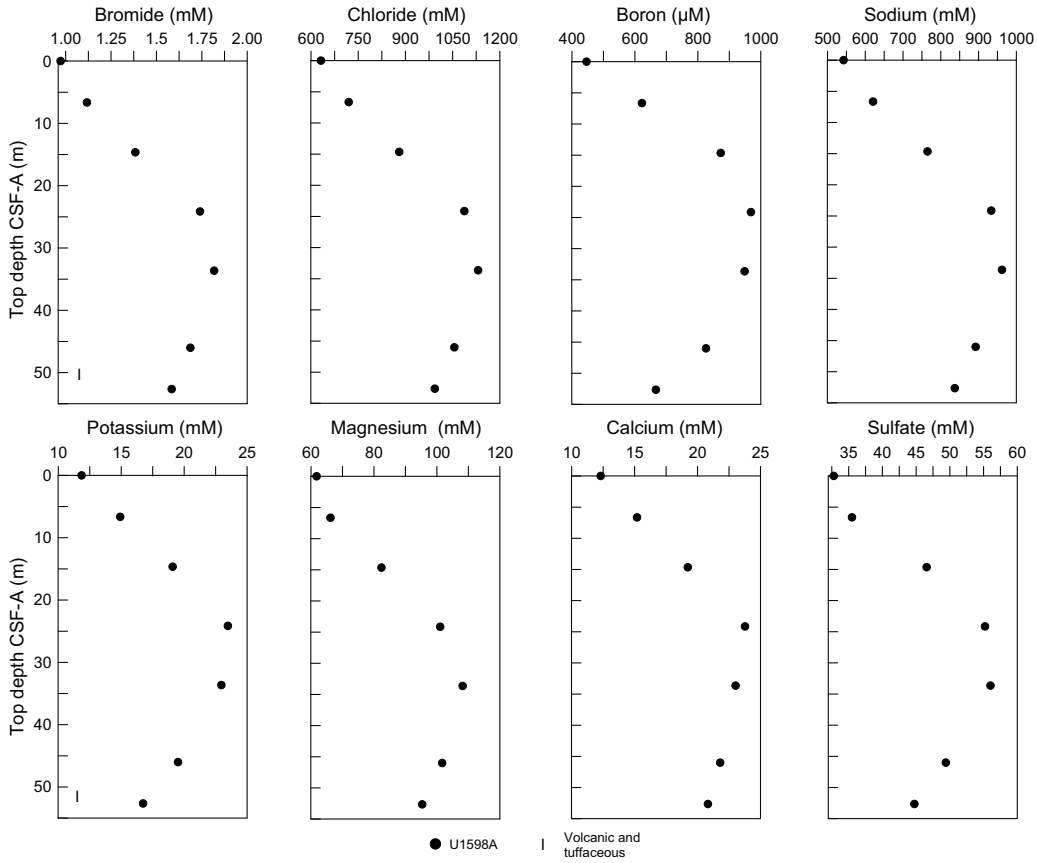

Figure F22. IC and ICP-AES concentrations of Br, Cl, B, Na, K, Mg, Ca, and SO_4^{2-} in IW samples, Site U1598. Lithostratigraphic Unit I is described in Lithostratigraphy.

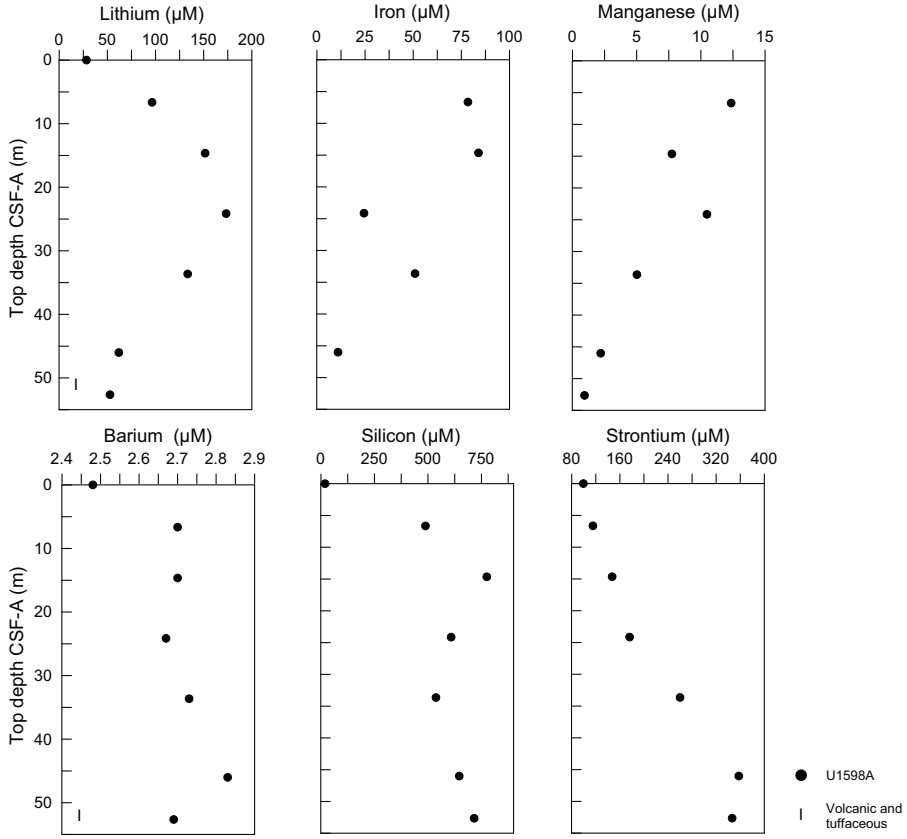

Figure F23. ICP-AES concentrations of Li, Fe, Mn, Ba, Si, and Sr in IW samples, Site U1598. Lithostratigraphic Unit I is described in Lithostratigraphy.

Table T15. Total inorganic carbon (TIC), percent $CaCO_3$, total carbon (TC), total nitrogen (TN), and TOC data, Site U1598. **Download table in CSV format.**

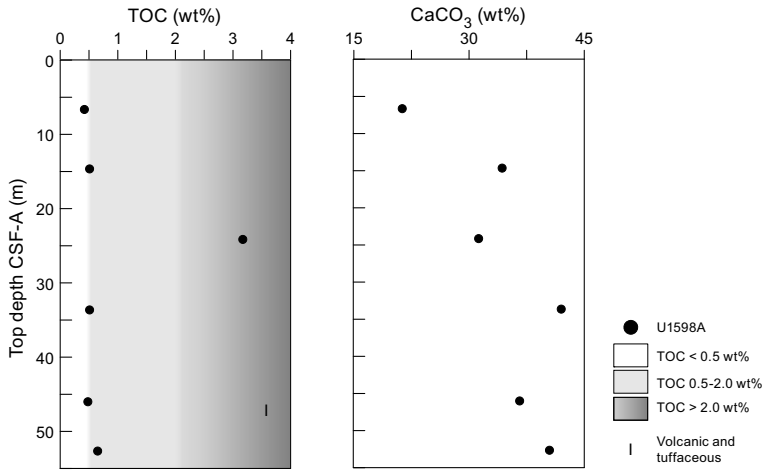

Figure F24. TOC and carbonate, Site U1598. Lithostratigraphic Unit I is described in Lithostratigraphy. Sapropel conventions follow Kidd et al. (1978).

References

Aarburg, S., and Frechen, M., 1999. Die pyroklastischen Abfolgen der Christiana-lnseln (Süd-Ägäis, Griechenland). In Becker-Haumann, R., and Frechen, M. (Eds.) Terrestrische Quartargeologie. 260–276.

Backman, J., Raffi, I., Rio, D., Fornaciari, E., and Pälike, H., 2012. Biozonation and biochronology of Miocene through Pleistocene calcareous nannofossils from low and middle latitudes. Newsletters on Stratigraphy, 45(3):221–244. **https://doi.org/10.1127/0078-0421/2012/0022**

Di Stefano, A., and Sturiale, G., 2010. Refinements of calcareous nannofossil biostratigraphy at the Miocene/Pliocene Boundary in the Mediterranean region. Geobios, 43(1):5–20. **https://doi.org/10.1016/j.geobios.2009.06.007**

Druitt, T., Kutterolf, S., and Höfig, T.W., 2022. Expedition 398 Scientific Prospectus: Hellenic Arc Volcanic Field. International Ocean Discovery Program. **https://doi.org/10.14379/iodp.sp.398.2022**

Druitt, T.H., Kutterolf, S., Ronge, T.A., Beethe, S., Bernard, A., Berthod, C., Chen, H., Chiyonobu, S., Clark, A., DeBari, S., Fernandez Perez, T.I., Gertisser, R., Hübscher, C., Johnston, R.M., Jones, C., Joshi, K.B., Kletetschka, G., Koukousioura, O., Li, X., Manga, M., McCanta, M., McIntosh, I., Morris, A., Nomikou, P., Pank, K., Peccia, A., Polymenakou, P.N., Preine, J., Tominaga, M., Woodhouse, A., and Yamamoto, Y., 2024a. Site U1589. In Druitt, T.H., Kutterolf, S., Ronge, T.A., and the Expedition 398 Scientists, Hellenic Arc Volcanic Field. Proceedings of the International Ocean Discovery Program, 398: College Station, TX (International Ocean Discovery Program). **https://doi.org/10.14379/iodp.proc.398.103.2024**

Druitt, T.H., Kutterolf, S., Ronge, T.A., Beethe, S., Bernard, A., Berthod, C., Chen, H., Chiyonobu, S., Clark, A., DeBari, S., Fernandez Perez, T.I., Gertisser, R., Hübscher, C., Johnston, R.M., Jones, C., Joshi, K.B., Kletetschka, G., Koukousioura, O., Li, X., Manga, M., McCanta, M., McIntosh, I., Morris, A., Nomikou, P., Pank, K., Peccia, A., Polymenakou, P.N., Preine, J., Tominaga, M., Woodhouse, A., and Yamamoto, Y., 2024b. Site U1591. In Druitt, T.H., Kutterolf, S., Ronge, T.A., and the Expedition 398 Scientists, Hellenic Arc Volcanic Field. Proceedings of the International Ocean Discovery Program, 398: College Station, TX (International Ocean Discovery Program). **https://doi.org/10.14379/iodp.proc.398.105.2024**

Fisher, R.V., and Schmincke, H.-U., 1984. Pyroclastic Rocks: Berlin (Springer). **https://doi.org/10.1007/978-3-642-74864-6**

Gradstein, F.M., Ogg, J.G., Schmitz, M.D., and Ogg, G.M. (Eds.), 2020. The Geologic Time Scale 2020: Amsterdam (Elsevier BV). **https://doi.org/10.1016/C2020-1-02369-3**

Hayward, B.W., Grenfell, H.R., Reid, C.M., and Hayward, K.A., 1999. Recent New Zealand shallow-water benthic foraminifera: taxonomy, ecologic distribution, biogeography, and use in paleoenvironmental assessment. In Institute of Geological & Nuclear Sciences Monograph, 21: Lower Hutt, NZ.

Jutzeler, M., White, J.D.L., Talling, P.J., McCanta, M., Morgan, S., Le Friant, A., and Ishizuka, O., 2014. Coring disturbances in IODP piston cores with implications for offshore record of volcanic events and the Missoula megafloods. Geochemistry, Geophysics, Geosystems, 15(9):3572–3590. **https://doi.org/10.1002/2014GC005447**

Keller, J., Dietrich, V., Reusser, E., Gertisser, R., and Aarburg, S., 2010. Recognition of a major ignimbrite in the early evolution of the Santorini Group: the Christiani Ignimbrite. Presented at the Cities on Volcanoes Conference, Tenerife, Spain, January 2010.

Kidd, R.B., Cita, M.B., and Ryan, W.B.F., 1978. Stratigraphy of eastern Mediterranean sapropel sequences recovered during DSDP Leg 42A and their paleoenvironmental significance. In Hsü, K., Montadert, L., et al., Initial Reports of the Deep Sea Drilling Project. 42(1): Washington, DC (US Government Printing Office), 421–443. **https://doi.org/10.2973/dsdp.proc.42-1.113-1.1978**

Kutterolf, S., Druitt, T.H., Ronge, T.A., Beethe, S., Bernard, A., Berthod, C., Chen, H., Chiyonobu, S., Clark, A., DeBari, S., Fernandez Perez, T.I., Gertisser, R., Hübscher, C., Johnston, R.M., Jones, C., Joshi, K.B., Kletetschka, G., Koukousioura, O., Li, X., Manga, M., McCanta, M., McIntosh, I., Morris, A., Nomikou, P., Pank, K., Peccia, A., Polymenakou, P.N., Preine, J., Tominaga, M., Woodhouse, A., and Yamamoto, Y., 2024. Expedition 398 methods. In Druitt, T.H., Kutterolf, S., Ronge, T.A., and the Expedition 398 Scientists, Hellenic Arc Volcanic Field. Proceedings of the International Ocean Discovery Program, 398: College Station, TX (International Ocean Discovery Program). **https://doi.org/10.14379/iodp.proc.398.102.2024**

Kutterolf, S., Freundt, A., Hansteen, T.H., Dettbarn, R., Hampel, F., Sievers, C., Wittig, C., Allen, S.R., Druitt, T.H., McPhie, J., Nomikou, P., Pank, K., Schindlbeck-Belo, J.C., Wang, K.-L., Lee, H.-Y., and Friedrichs, B., 2021. The medial offshore record of explosive volcanism along the central to eastern Aegean Volcanic Arc: 1. tephrostratigraphic correlations. Geochemistry, Geophysics, Geosystems, 22(12):e2021GC010010. **https://doi.org/10.1029/2021GC010010**

Le Maitre, R.W., Steckeisen, A., Zanettin, B., Le Bas, M.J., Bonin, B., and Bateman, P. (Eds.), 2002. Igneous Rocks: A Classification and Glossary of Terms (Second edition): Cambridge, UK (Cambridge University Press). **https://doi.org/10.1017/CBO9780511535581**

Lirer, F., Foresi, L.M., Iaccarino, S.M., Salvatorini, G., Turco, E., Cosentino, C., Sierro, F.J., and Caruso, A., 2019. Mediterranean Neogene planktonic foraminifer biozonation and biochronology. Earth-Science Reviews, 196:102869. **https://doi.org/10.1016/j.earscirev.2019.05.013**

Martini, E., 1971. Standard Tertiary and Quaternary calcareous nannoplankton zonation. Proceedings of the Second Planktonic Conference, Roma, 1970:739–785.

Okada, H., and Bukry, D., 1980. Supplementary modification and introduction of code numbers to the low-latitude coccolith biostratigraphic zonation (Bukry, 1973; 1975). Marine Micropaleontology, 5(3):321–325. **https://doi.org/10.1016/0377-8398(80)90016-X**

Pimmel, A., and Claypool, G., 2001. Introduction to shipboard organic geochemistry on the JOIDES Resolution. Ocean Drilling Program Technical Note, 30. **https://doi.org/10.2973/odp.tn.30.2001**

Preine, J., Karstens, J., Hübscher, C., Crutchley, G.J., Druitt, T.H., Schmid, F., and Nomikou, P., 2022a. The hidden giant: how a rift pulse triggered a cascade of sector collapses and voluminous secondary mass-transport events in the early evolution of Santorini. Basin Research, 34(4):1465–1485. **https://doi.org/10.1111/bre.12667**

Preine, J., Karstens, J., Hübscher, C., Nomikou, P., Schmid, F., Crutchley, G.J., Druitt, T.H., and Papanikolaou, D., 2022b. Spatio-temporal evolution of the Christiana-Santorini-Kolumbo volcanic field, Aegean Sea. Geology, 50(1):96–100. **https://doi.org/10.1130/G49167.1**

Rio, D., Raffi, I., and Villa, G., 1990. Pliocene-Pleistocene calcareous nannofossil distribution patterns in the western Mediterranean. In Kastens, K.A., Mascle, J., et al., Proceedings of the Ocean Drilling Program, Scientific Results. 107: College Station, TX (Ocean Drilling Program), 513–533. **https://doi.org/10.2973/odp.proc.sr.107.164.1990**

Tsampouraki-Kraounaki, K., and Sakellariou, D., 2018. Seismic stratigraphy and geodynamic evolution of Christiana Basin, South Aegean Arc. Marine Geology, 399:135–147. **https://doi.org/10.1016/j.margeo.2018.02.012**